31st Congress of the International Council of the Aeronautical Sciences

Belo Horizonte, Brazil; September 09-14, 2018

A RAPID AERODYNAMIC PREDICTION METHOD FOR UNCONVENTIONAL TRANSONIC AIRCRAFT CONFIGURATIONS

Simon Prince*, Davide Di Pasquale*, Kevin Garry* & Cristina Nuzzo**
***Cranfield University, UK, ****Politecnico di Torino, Italy**

Keywords: *Transonic Aerodynamics, Aircraft Design, CFD*

Abstract

This paper presents some results comparing the use of the Full Potential equations, coupled with the turbulent integral boundary layer equations for aircraft transonic cruise analysis. Use of such a method in the conceptual design stage is shown to be capable of yielding accurate enough data in a few minutes on a single processor, where Navier-Stokes simulations on 100+ processors take several days.

1 Introduction

Modern conceptual aircraft design requires the rapid generation of approriate aerodynamics data for performance calculation and structural analysis within the context of trade-off studies. Such data must be of sufficient accuracy, in terms of overall and local lift and drag forces, that the performance trends are correctly captured and such attributes as range and fuel burn characteristics are predicted accurately.

The need for this data to be available rapidly to allow for many concepts and configurations to be assessed in these trade-off studies allows the costs of the conceptual design stage to be minimized. The accuracy of the analysis methods allows uncertainties associated with the decision making and the resulting conceptual configurations to be minimized, thereby reducing the downstream costs associated with design mistakes.

The focus of this paper is the demonstration of a rapid, lower fidelity method for the conceptual design and analysis of transonic cruise transport aircraft. Since the application of interest is the design analysis of transonic cruise wing flows, the Viscous Full Potential (VFP) method, which couples the solution of the Full Potential equations for compressible rotational inviscid flow with the integral boundary layer equations, is wholly adequate for a design method. No aircraft wing would be designed to operate in cruise flight under significant separated flow condition, which would result in buffet phenomena, and so a rapid and relatively accurate "attached flow" method for such applications is valid.

2 The Viscous Full Potential Method

2.1 The Governing Equations

Potential flow methods involve the solution of the governing equations which are reduced by assuming the flow is inviscid, irrotational and isentropic. These simplifications allow the continuity equation to be derived in terms of the velocity potential function Φ. The last two assumptions, however, limit the validity of the method to cases where no shock waves exist in the flow field, or where the shock waves are so weak that the isentropic assumption leads to only minor errors in the calculation of pressure and velocity. Supersonic flows can be computed only in the regions inside a shock layer. An example would be the supersonic flow around a slender body, where a potential flow solution could be computed between the attached bow shock wave and the body surface, assuming the conditions on the downstream side of the shock surface can be determined as a boundary condition for the calculation. The full velocity potential equation, for an irrotational, inviscid, isentropic flow, in terms of Cartesian coordinates (x,y,z) is written:

$$\left(1-\frac{\bar{\Phi}_x^2}{a^2}\right)\bar{\Phi}_{xx}+\left(1-\frac{\bar{\Phi}_y^2}{a^2}\right)\bar{\Phi}_{yy}+\left(1-\frac{\bar{\Phi}_z^2}{a^2}\right)\bar{\Phi}_{zz}$$

$$-2\frac{\bar{\Phi}_x\bar{\Phi}_y}{a^2}\bar{\Phi}_{xy}-2\frac{\bar{\Phi}_x\bar{\Phi}_z}{a^2}\bar{\Phi}_{xz}-2\frac{\bar{\Phi}_y\bar{\Phi}_z}{a^2}\bar{\Phi}_{yz}$$

$$-2\bar{\Phi}_x\bar{\Phi}_{xt}-2\bar{\Phi}_y\bar{\Phi}_{yt}-2\bar{\Phi}_z\bar{\Phi}_{zt}-\bar{\Phi}_{tt}=0 \quad (1)$$

where the velocity potential Φ is defined by:

$$V=\sqrt{u^2+v^2+w^2}=\nabla\bar{\Phi} \quad (2)$$

such that:

$$u=\bar{\Phi}_x=\frac{\partial\bar{\Phi}}{\partial x},\ v=\bar{\Phi}_y=\frac{\partial\bar{\Phi}}{\partial y},\ w=\bar{\Phi}_z=\frac{\partial\bar{\Phi}}{\partial z} \quad (3)$$

and the time, t, is in the unsteady terms. If the flow is steady, the last four terms of the equation are neglected.

2.2 The VFP solver implementation

For this application, a steady flow VFP solver has been used, which is a development of the VFP code available commercially from IHS ESDU [1]. This code allows the wing geometry to be input as a series of section profiles to be defined from the root to the tip, along with the corresponding location, relative to the fuselage reference point, of the local leading edge, the chord length and the local twist angle setting. The process of changing such geometric features as leading edge sweep, taper, local dihedral, crank location and twist setting therefore involves the change of a few parameters, which can be done manually or as part of a computational optimization algorithm.

The VFP program also incorporates the modelling of the zero alpha flow around the isolated fuselage whereby the potential flow field is obtained by the classical solution of the Stokes-streamline problem for the input body geometry defined in a separate input file [2]. This provides both the zero incidence surface pressure distribution on the isolated fuselage, and the increment in Mach number at the wing quarter chord location across the wing span which is used to vary the local Mach number along the wing span in the VFP calculation. Validations of this method are reported in reference [3]. In order to calculate the aerodynamic characteristics of a complete wing-body configuration, the contribution to the forces and moments from the fuselage is calculated by computing the surface pressure distribution at the required angle of attack by slender body theory [4]. The surface integration of this distribution provides the local distribution of the lift and drag pressure force along its longitudinal axis (x in this case) which is further integrated to provide the total lift, drag and pitching moment contribution from the fuselage. The interference from the wing flow onto the body is not yet accounted for in the method, but this is deemed to be relatively minor for the long fuselage configurations typical of modern transport aircraft.

The VFP code automatically generates the separate computational grids around both the fuselage and the wing, details for which are provided in ref [1]. For this study the wing-bodies investigated are modelled with meshes of 135,432 cells, wrapping an O-topology grid around the wing (in this case 162 cells wrapped around the wing, 38 cells along the span of the wing and 22 cells outward from the wing surface). The fuselage was modelled with 33 points along its axis, and 32 points around its circular half perimeter, where the flow is assumed be to symmetric about the y = 0 (wing centreline) plane.

The code then solves the full (non-linear) potential flow equations, coupled with the integral boundary layer equations. In particular the code uses a relaxation algorithm to solve the finite difference form of the full velocity-potential equation which is coupled with the semi-inverse, swept / tapered integral boundary layer method of Ashill and Smith [5, 6]. The convergence criteria was set as a maximum absolute change in value of velocity perturbation potential reduced to an order of 10^{-6}.

2.3 The Navier-Stokes solver

For comparison with the VFP results, a modern commercial, compressible flow, Navier-Stokes

solver was employed to obtain high resolution simulations of the flows analyzed with the VFP method. The solver employed the Roe approximate Riemann solver for shock capturing with a second order scheme in both space and time to obtain converged steady flow solutions. A number of turbulence models were used for the Reynolds Averaged Navier-Stokes (RANS) calculations for comparative purposes, as detailed in the paper, and for test case 2 the Delayed Detached Eddy Simulation (DDES) method was used to obtain unsteady time accurate data. Grid insensitivity was demonstrated in all cases, the convergence criteria being overall force coefficient convergence together with residual convergence to at least 10^{-4}.

3 The Test Cases

3.1 Test Case 1: The W4 Wing-Body Configuration

The first validation test case was the RAE Wing 4, transonic wing-body configuration as shown in fig 1, which was tested in the RAE Bedford 8ft Supersonic wind tunnel in the late 1970's.

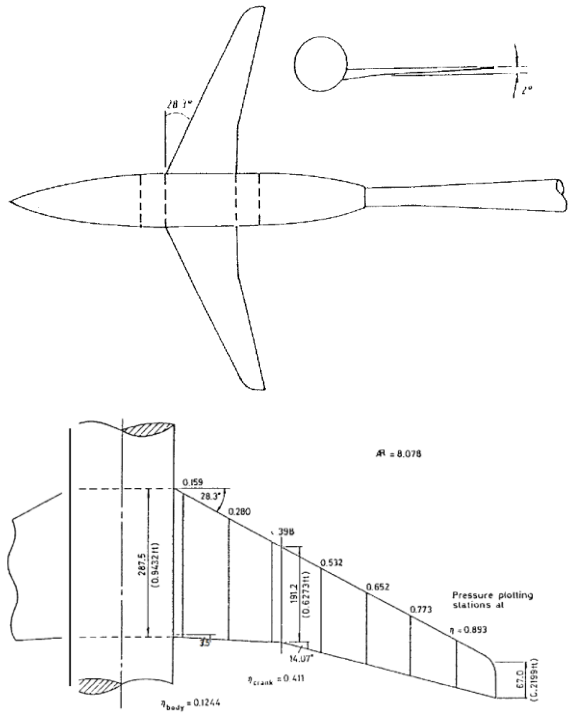

Fig 1: Dimensions of the V4 wing-body configuration [7].

The data was made available via the NATO AGARD AR-303 report in 1994 [7]. In this paper, comparisons are presented for the Mach 0.78, Re_c = 5.12x10^6 condition.

3.2 Test Case 2: The RBC12 Wing-Body Configuration

The configuration chosen for the second validation test case was the RBC12 wing/body geometry designed by the Aircraft Research Association (ARA). Fig 2 presents a photograph of the half model being tested in the ARA Transonic Wind Tunnel along with some basic dimensions [8]. The RBC12 model has a quarter chord sweep of 25º, with a swept / tapered and cranked planform which has a semi-span of 1.085m, a mean aerodynamic chord of 0.279m, and an aspect ratio of 7.78.

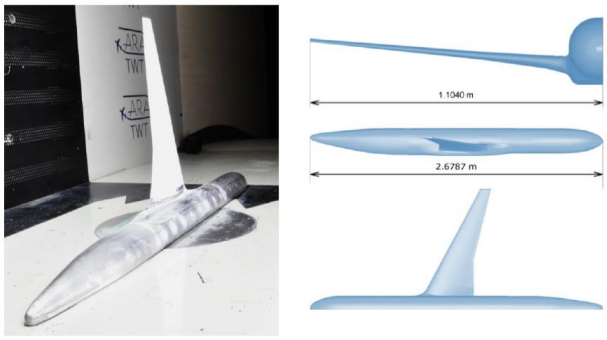

Fig 2: The RBC12 wing-body configuration half model in the ARA Transonic Wind Tunnel, and its principle dimensions [8].

The half span model was mounted on the floor of the tunnel, from a 5-component strain guage balance which measured the forces and moments on the combined wing and fuselage. Surface pressures were obtained using the Dynamic Pressure Sensitive Paint (DPSP) method. Tests were conducted in the Mach number range 0.7 – 0.84, corresponding to Reynolds numbers, based on mean aerodynamic chord, of 2.8 to 3.9 million. In this paper only the comparisons for the Mach 0.8, Re_c = 3.75x10^6 condition are presented.

3.3 Test Case 3: The BW-11 Blended Wing-Body Configuration

The VFP method having been validated against experimental data with test cases 1 and 2, the third demonstration was to assess the ability of the VFP approach to accurately and rapidly predict the aerodynamic characteristics of a transonic blended wing body configuration. For this the Cranfield University BW-11 configuration was adopted, the basic dimensions for which are presented in Fig 3.

Because experimental data for such configurations at transonic flight conditions, at the time of writing, were not available to the authors, it was decided to make a direct comparison between VFP and high resolution Reynolds Averaged Navier-Stokes results, given that this approach has been shown to be accurate enough for conceptual design analysis for this application, as will be demonstrated for the first two test cases.

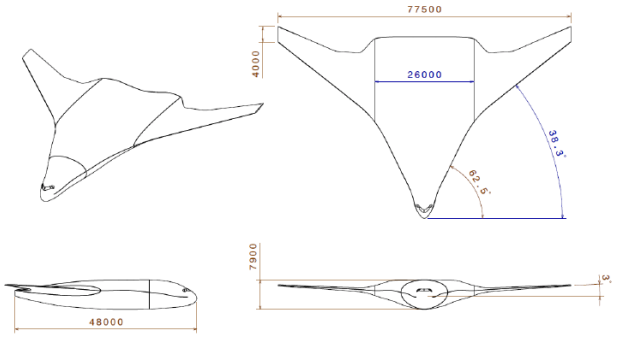

Fig 3: Dimensions of the basic Cranfield BW-11 Blended Wing Body configuration with no winglets (units in mm).

4 Results and Discussion

4.1 Test Case 1: The W4 Wing-Body Configuration

For this test case the VFP results are compared only with the experimental data for the Mach 0.78 case of interest. No RANS calculations were performed for this case. Fig 4 compares the VFP predicted lift (C_L) and drag (C_D) coefficient characteristics with those obtained from the experiment. Here the dashed line in the lift curve indicates the linear trend in VFP predicted lift and shows that this lower order method has successfully captured the non-linearity at the higher α associated with onset trailing edge separations which the coupled boundary layer method can capture. While the VFP method is seen to resolve the drag levels at low α remarkably well, it over-predicts C_D by up to 10 drag counts at the higher incidences. For a lower fidelity method, however, this is still acceptable as it is often the trends which need to be resolved and not necessarily accurate magnitudes.

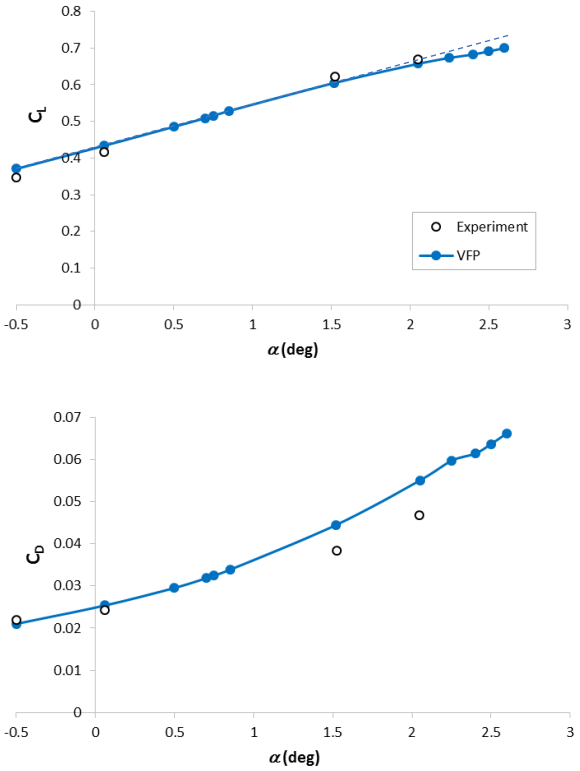

Fig 4: Comparison of measured and computed lift and drag characteristics with α, for W4. M_∞=0.78, Re_c=5.12x10^6.

The VFP method outputs automatically, a breakdown of the local lift and drag contributions along the wing span for the assessment of wing loading. Fig 5 presents the comparison between the VFP predicted wing loadings and those obtained from integration of the experimentally measure surface pressures. Here, again, the VFP method is seen to capture these remarkably well for all four α cases investigated, certainly to an accuracy useful at the conceptual design stage.

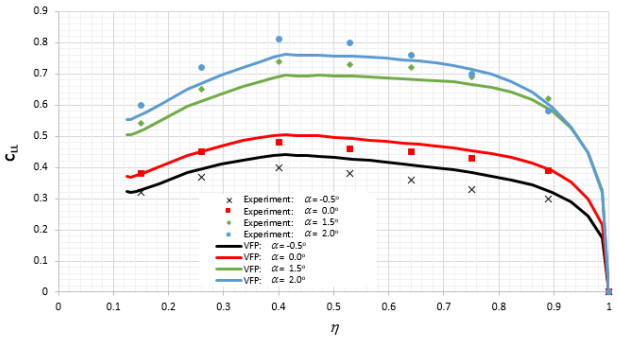

Fig 5: Comparison of the variation with angle of attack of measured (via integrated surface pressure) and VFP predicted spanwise loading (local lift coefficient). M_∞=0.78, Re_c=5.12x10^6.

A selection of the comparisons of the predicted and experimentally measured chordwise surface pressure distributions are presented at different spanwise stations in figure 6 and 7, for α = 0 and 2.0^o respectively. Here, η is the span location as a percentage of the total wing span, and C_p is the local surface pressure coefficient. For the zero incidence case, shown in fig 6, the surface pressure distributions are captured with an accuracy typically expected with a Navier-Stokes calculation, including the resolution of the weak upper surface shock wave, towards the wing tip around 30% chord. The discrepancy with the two experimental points for the most inboard spanwise location is due to a known experimental measurement error.

For the more challenging case of α = 2.0^o, where a relatively strong upper surface shock wave appears, the comparisons are plotted in fig 7. Here, again, the VFP method provides predicted surface pressure distributions, with indicative shock wave locations and strengths that are typical of the accuracy expected of modern Navier-Stokes solvers using much finer computational meshes and at much higher computational and run-time cost. The plot for the most outboard spanwise station is of interest, as this shows that the VFP method has successfully captured the trend towards boundary layer separation at the tip, indicated when local C_p at the trailing edge goes negative.

The VFP method has been developed to output both the local boundary layer properties on the wing surface, including the displacement thickness, δ^*, the momentum thickness, θ, the shape factor, $\bar{H}$ $(= \delta^*/\theta)$, together with local skin friction coefficient, C_f, and the skew angle, β, between the limiting flow vector above the surface, and that at the boundary layer edge, which is useful for the design of flow control devices.

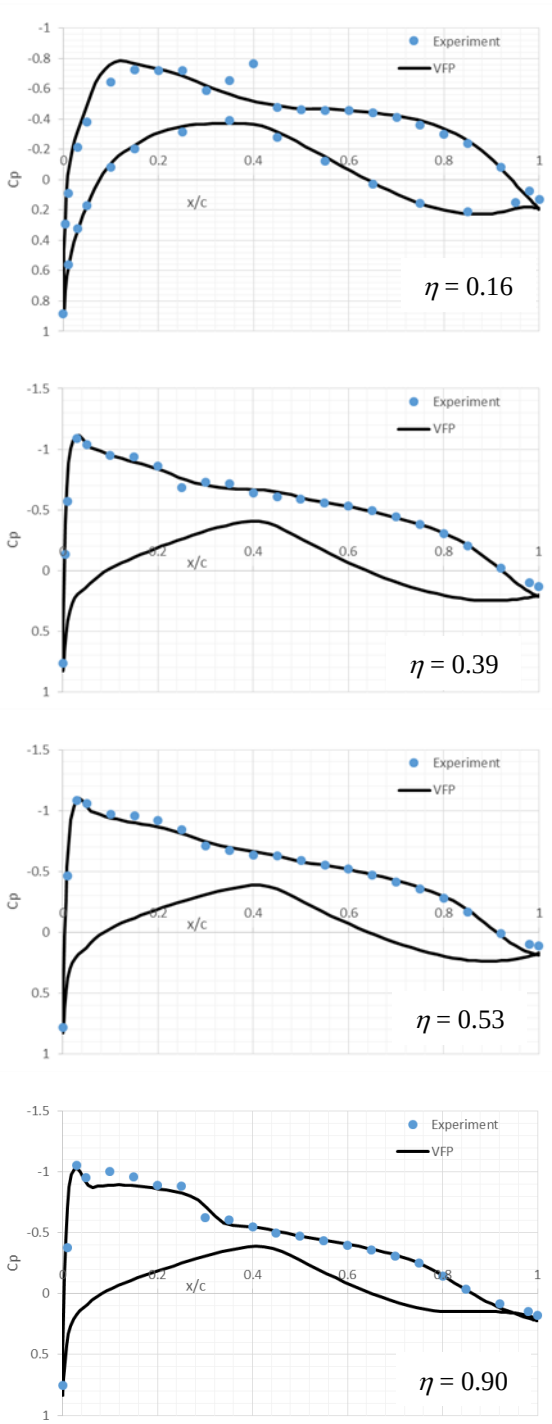

Fig 6: Comparison of measured and computed surface pressure distributions for W4. M_∞=0.78, α = 0.0^o, Re_c=5.12x10^6.

These parameters are output directly from the boundary layer solver, whereas separate post-processing is required from a CFD solver. Fig 8 presents the VFP derived upper surface C_p contours showing the resolution for two α cases.

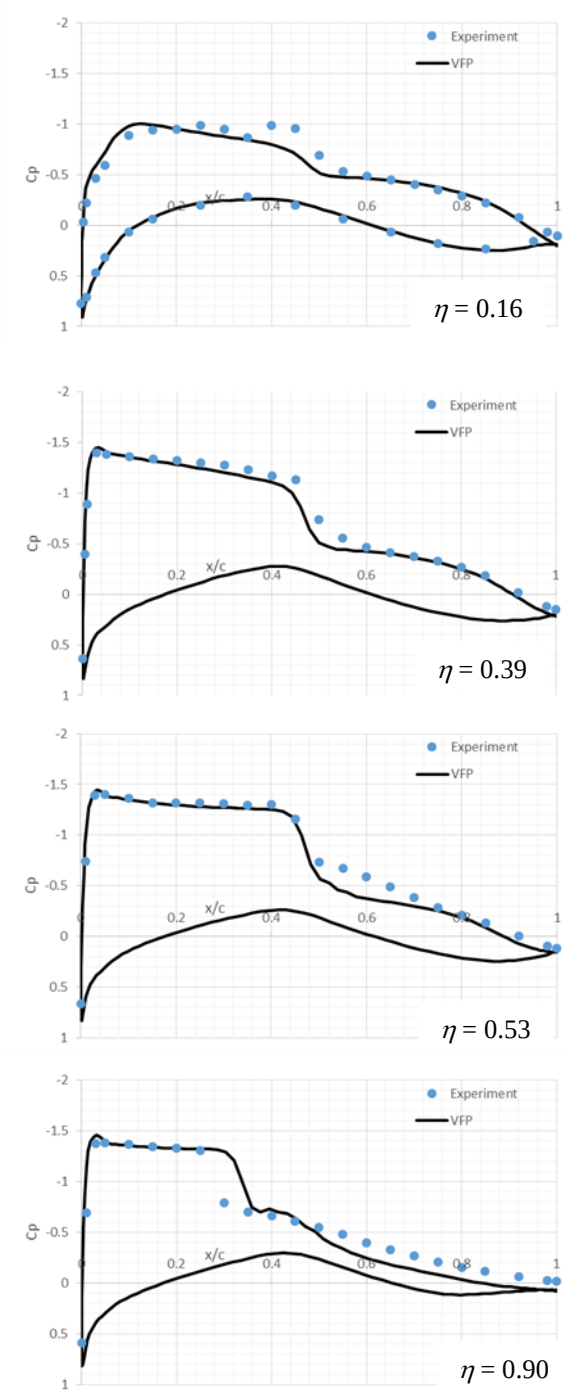

Fig 7: Comparison of measured and computed surface pressure distributions for W4. M_∞=0.78, α = 2.0°, Re_c=5.12x10^6.

The lower α case correctly resolves a shock free upper surface flow, while a strong swept shock wave is well resolved for the 2.5° incidence case. The shock wave is correctly seen to be the weakest inboard, strengthening outboard with a noticeable unsweep towards the tip where incipient boundary layer separation is known to occur.

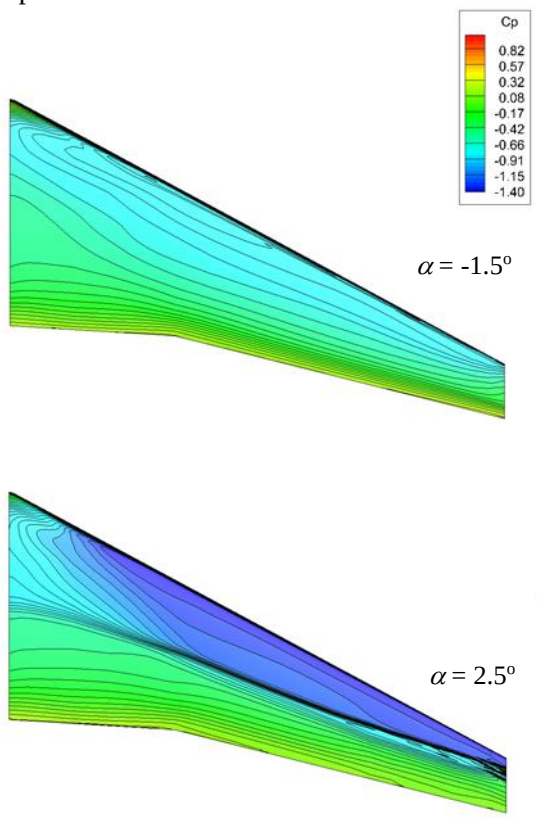

Fig 8: Selected VFP computed upper surface C_p contours for W4. M_∞=0.78, Re_c=5.12x10^6.

4.2 Test Case 2: The RBC12 Wing-Body Configuration

For test case 2 the VFP predictions were compared against both experimental data as well as high fidelity CFD, which in this case involved Delayed Detached Eddy Simulation (DDES) as part of another study of this test case. Fig 9 presents the surface mesh for the coarsest structured grid superimposed with the resulting surface C_p contours for the Mach 0.8, zero incidence, case of interest. Grid convergence was found (force coefficients to 3 significant figures) for cell counts of the order of ~20 million. Individual calculations involving the acquisition of 0.5 seconds of simulated flow took typically 15 days of run-time on 128 core processors of a

modern parallel cluster machine. The steady RANS (k-ω SST turbulence model) calculation from which the DDES simulation was started from took about 1 day for convergence to be achieved on the same computing resource. Compare this with a ~120 second run time for a corresponding VFP calculation on a single processor of a modest desktop PC.

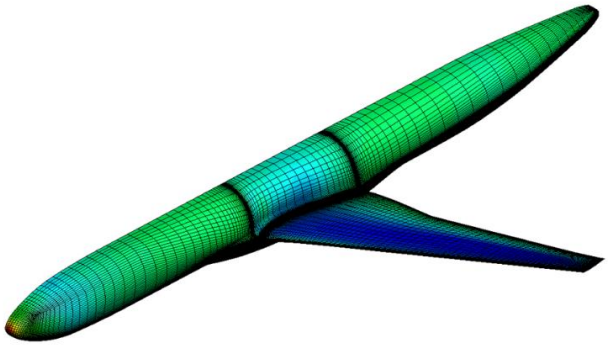

Fig 9: The coarse RBC12 structured surface grid, with surface C_p contours for the Mach 0.8, α=0^o case.

Fig 10 compares the lift and drag characteristics for both the VFP prediction and the initial RANS calculation (3 points only), with the corresponding experimental measurements [8]. Data for both the wing-alone and for the combined wing and fuselage are plotted for the predicted results.

Both the VFP and the RANS calculation resolve the lift and drag coefficients remarkably well at α =2.5^o. The VFP result correctly resolves the non-linearity in the lift trend due the onset of shock induced viscous effects, together with the associated rise in drag. If anything the VFP slightly over-predicted the lift force which thereby resulted in excessive induced drag and a corresponding over-prediction in drag force compared with experiment. The RANS predicted lift is seen to follow the continued linear trend (dashed line), while the drag coefficient at the highest α was woefully under-predicted. Fig 11, which compares the experimentally measured (dynamic pressure sensitive paint) upper surface static pressure contours with the corresponding predicted results for the higher α case, provides a possible answer to this failure of the RANS/DDES method.

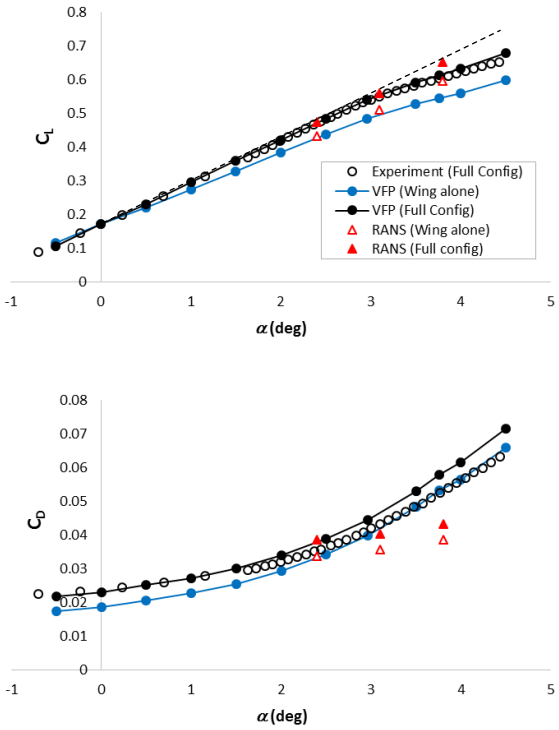

Fig 10: Comparison of measured and computed lift and drag characteristics with α, for RBC12.

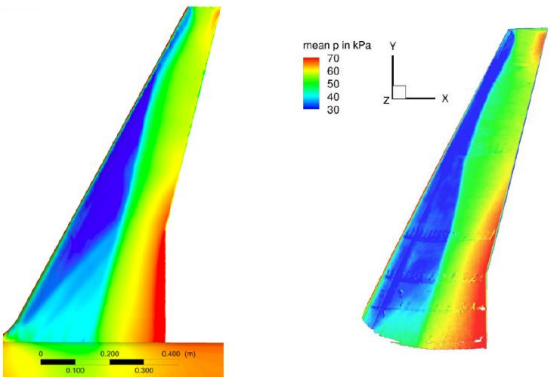

a) DDES *b) Experiment [8]*

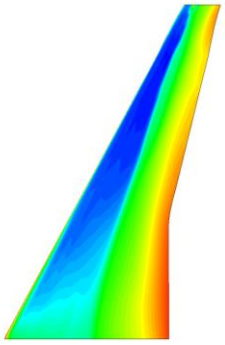

c) VFP

Fig 11: Comparison of measured and computed surface pressure contours for RBC12. M_∞=0.8, α = 3.76^o, Re_c=3.75x10^6.

Close scrutiny of the pressure contours at the tip indicates that the time averaged DDES result (almost identical to the RANS result) predicts a much weaker upper surface shock wave, which sits closer to the leading edge, whilst the VFP result predicts a stronger shock sitting further rearward, with a considerable unsweep at the tip, as seen in the experiment. The VFP method solves the coupled turbulent boundary layer equations directly, while the CFD method solves approximate equations for the flow and the turbulence production and dissipation which almost certainly has resulted, in this case, in poor boundary layer resolution and corresponding shock evolution towards the tip leading edge.

A selection of the output from the VFP solver for the characterization of the local chordwise pressure and boundary layer state for the inboard spanwise station, η=0.1, is presented in fig 12. This is typical of the data that is produced and which can be quickly used to aid in deciding how a given wing may be redesigned for improved performance or for safer off-design characteristics. Such a method, for which an entire pitch sweep can be obtained in less than an hour on a modest desktop machine, clearly lends itself well to the conceptual design activity, where it would be unwise to deploy high resolution Navier-Stokes methods.

4.3 Test Case 3: The BW-11 Blended Wing-Body Configuration

For test case 3 the comparisons are only between VFP and Navier-Stokes predictions at an arbitrary Reynolds number, based on centre-span chord, of 9 million.

Fig. 13 presents the surface mesh density for the RANS calculations, where the hybrid grid encompassed ~14 million cells, and that used in the VFP calculation which comprised 135,432 cells. The RANS grid used a layer of 30 prismatic cells to model the boundary layer, where y^+ was found to be in the range 1 – 10.

A comparison of the VFP and RANS predicted (with three different turbulence models) lift and drag characteristics is provided in figure 14 for M=0.75.

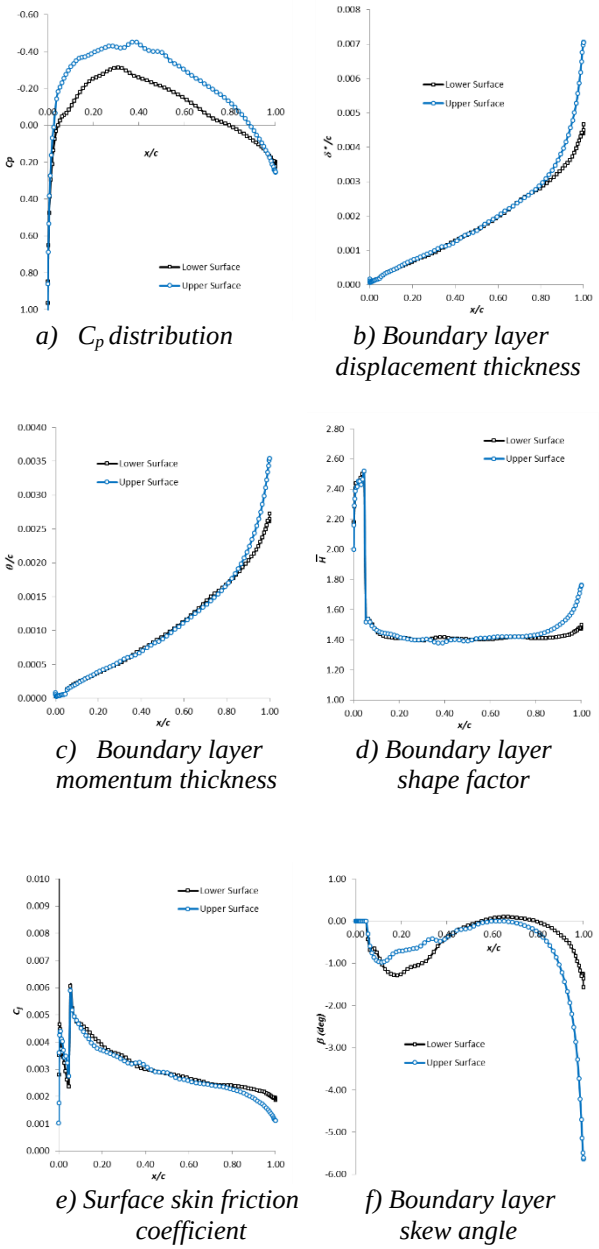

a) C_p distribution

b) Boundary layer displacement thickness

c) Boundary layer momentum thickness

d) Boundary layer shape factor

e) Surface skin friction coefficient

f) Boundary layer skew angle

Fig 12: VFP computed chordwise distribution of viscous flow characteristics for RBC12 at spanwise location η=0.1. M_∞=0.8, α = 3.76°, Re_c=3.75x10^6.

The VFP predicted lift has been found to be lower at the higher α, where leading edge vortex suction, resolved in the RANS solution, cannot be predicted by VFP which assumes attached boundary layer flow. The agreement between the VFP and RANS resolved drag coefficient is, however, remarkably good. For rapid prediction of leading edge vortex related loading, semi-empirical predictions of the contribution can be added to the predicted lift figure.

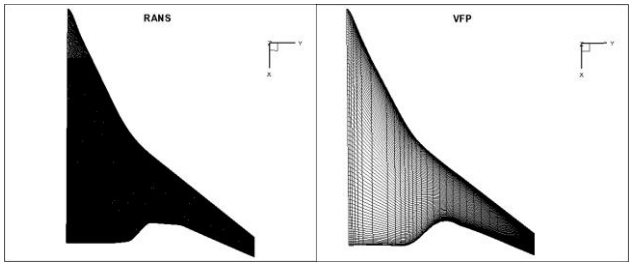

Fig 13: Comparison of the surface mesh densities used for the computational methods for the BW-11 predictions.

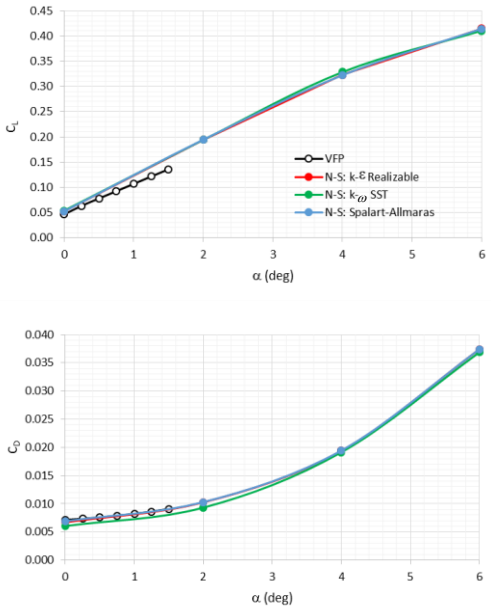

Fig 14: Comparison of the predicted lift and drag curves for BW-11. M_∞=0.75, Re_c=9x10^6.

Representative comparisons of the predicted upper surface pressure distributions at two Mach numbers are provided in fig. 15, which seems to demonstrate that the VFP method is successfully resolving the main flow characteristics including the large region of suction behind the wing leading edge crank, but fails to resolve the leading edge vortex suction on the forward fuselage. This is a focus for future improvement.

An important consideration in the design of blended wing-body aircraft is that of propulsion integration, for which an accurate set of data for the boundary layer characteristics on the upper rear fuselage is necessary if boundary layer ingesting intakes are employed. Here, the intake system must be carefully designed to minimize the degraded intake airflows arising from the ingestion of boundary layer air. Accurate boundary layer data is therefore essential for the conceptual design analysis of such an aircraft.

Fig. 16 presents the kind of boundary layer data that can be rapidly produced using the VFP method to aid in the understanding of the local flow condition in the region where a boundary layer ingesting propulsion system is to be installed. In this instance, turbulent boundary layer data is plotted on the upper surface at spanwise locations η = 0 (the body centerline) and η = 0.33 (just outboard of the leading edge crank) for the M =0.8, α =0^o condition.

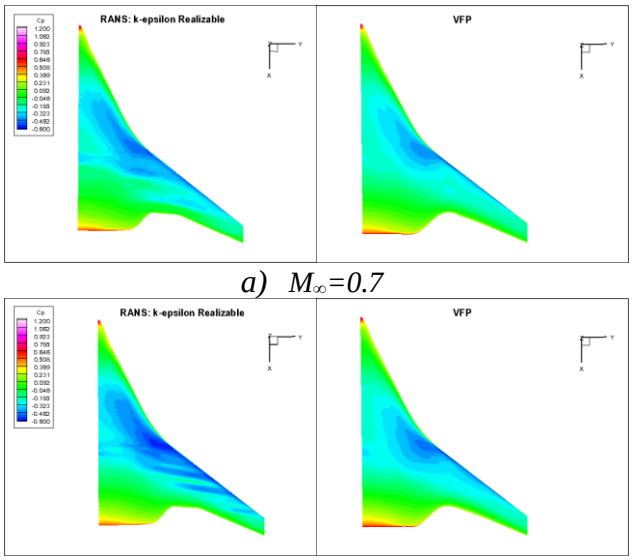

a) M_∞=0.7

b) M_∞=0.8

Fig 15: Comparison of the computed upper surface pressure contours for BW-11, α = 0^o, Re_c=9x10^6.

5 Conclusions

This paper, presenting some results of the feasibility assessment of using the Full Potential equations, coupled with the turbulent integral boundary layer equations, has demonstrated both the accuracy and the efficiency of the method for attach flow cases, prior to buffet onset, which are relevant to the transonic cruise condition. Use of such a method in the conceptual design stage is shown to be capable of yielding accurate enough data in a few minutes on a single processor, where Navier-Stokes simulations on 100+ processors can take several days.

Acknowledgements

This work was funded by Innovate UK and an Airbus UK led industrial consortia, as part of the ATI sponsored APROCONE project.

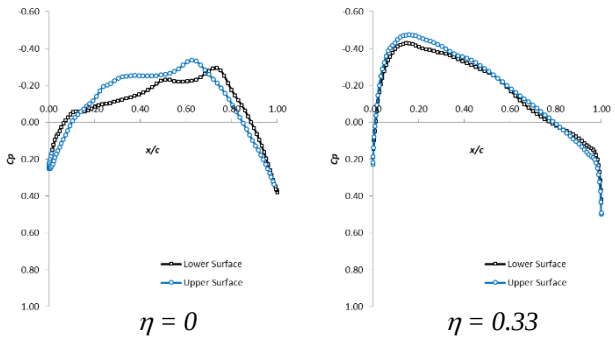

$\eta = 0$ $\eta = 0.33$

a) Cp distribution

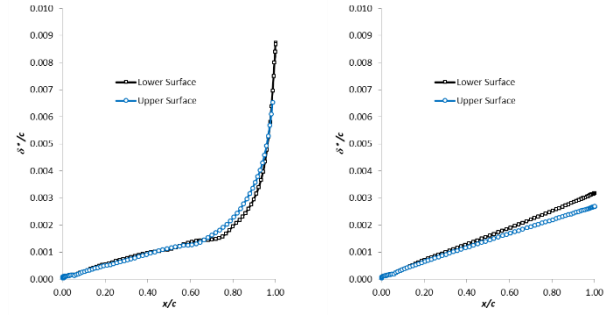

$\eta = 0$ $\eta = 0.33$

b) Boundary layer displacement thickness

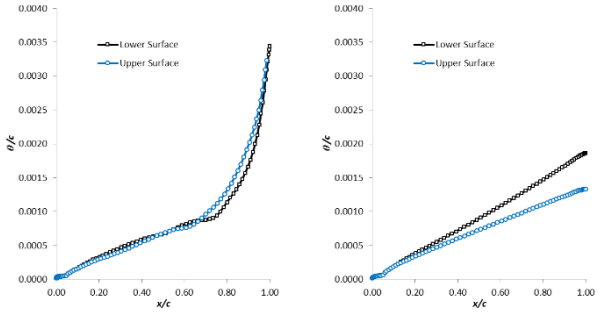

$\eta = 0$ $\eta = 0.33$

c) Boundary layer momentum thickness

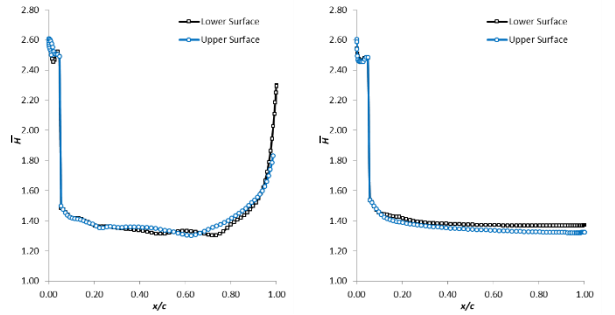

$\eta = 0$ $\eta = 0.33$

d) Boundary layer shape factor

Fig 16: VFP computed chordwise distribution of viscous flow characteristics for BW-11 at two spanwise locations. M_∞=0.8, α = 0°, Re_c=9x10^6.

References

[1] Full-potential (FP) method for three-dimensional wings and wing-body combinations – inviscid flow. Part I: Principles and results. ESDU 02013, June 2002 (with Amendment A, May 2006).

[2] Von Karman, T. "Calculation of pressure distribution on airship hulls" NACA TM 574, 1930.

[3] Viscous full-potential (VFP) method for three-dimensional wings and wing-body combinations. Part 1: Validation of VFP results with experiment and comparisons with other methods. ESDU 13013.

[4] De Jarnette, F. R., Ford, C. P. & Young, D. E. "A New Method for Calculating Surface Pressures on Bodies at an Angle of Attack in Supersonic Flow" AIAA Paper 79-1552. AIAA 12th Fluid & Plasma Dynamics Conference, Williamsburg, VA, July 1979.

[5] Ashill, P. R. & Smith, P. D. "An integral method for calculating the effects on turbulent boundary layer development on sweep and taper", RAE Technical Report, TR83053. June 1983.

[6] Smith, P.D. "A calculation method for the turbulent boundary layer on an infinite yawed wing in compressible, adiabatic flow. A.R.C. CP1268, 1974.

[7] J. L. Fulker, "Pressure distributions on research wing W4 mounted on an axisymmetric body", *AGARD AR 303*, Volume 2, 1994.

[8] Lawson, S. G, Greenwell, D. & Quinn, M. K. "Characterisation of Buffet on a Civil Aircraft Wing" AIAA Paper 2016-1309, *AIAA 54th Aerospace Sciences Meeting*, 4-8 Jan. 2016, San Diego, California, USA.

[9] Ashill, P. R & Smith, P. D. "An integral method for calculating the effects on turbulent boundary-layer development of sweep and taper", *RAE Technical Report*, TR83053, June 1983.

[10] Barnola, R. L. "Interaction between Aerodynamics, Structure and Packaging in a Blended Wing Body Configuration Conceptual Design", Cranfield University MSc Thesis, 2012.

Contact Author Email Address

mailto: simon.prince@cranfield.ac.uk

Copyright Statement